Dynamics of Wave Setup over a Steeply Sloping Fringing Reef

MARK L. BUCKLEY AND RYAN J. LOWE

School of Earth and Environment, and The Oceans Institute, and ARC Centre of Excellence for Coral Reef Studies, University of Western Australia, Crawley, Western Australia, Australia

JEFF E. HANSEN

School of Earth and Environment, and The Oceans Institute, University of Western Australia, Crawley, Western Australia, Australia

AP R. VAN DONGEREN

Unit ZKS, Department AMO, Deltares, Delft, Netherlands

ABSTRACT

High-resolution observations from a 55-m-long wave flume were used to investigate the dynamics of wave setup over a steeply sloping reef profile with a bathymetry representative of many fringing coral reefs. The 16 runs incorporating a wide range of offshore wave conditions and still water levels were conducted using a 1:36 scaled fringing reef, with a 1:5 slope reef leading to a wide and shallow reef flat. Wave setdown and setup observations measured at 17 locations across the fringing reef were compared with a theoretical balance between the local cross-shore pressure and wave radiation stress gradients. This study found that when radiation stress gradients were calculated from observations of the radiation stress derived from linear wave theory, both wave setdown and setup were underpredicted for the majority of wave and water level conditions tested. These underpredictions were most pronounced for cases with larger wave heights and lower still water levels (i.e., cases with the greatest setdown and setup). Inaccuracies in the predicted setdown and setup were improved by including a wave-roller model, which provides a correction to the kinetic energy predicted by linear wave theory for breaking waves and produces a spatial delay in the wave forcing that was consistent with the observations.

1. Introduction

Wave setup, or the increase in mean water level due to breaking waves, often represents a substantial portion of the total water depth over shallow coral reefs, and spatial gradients in setup are a primary driver of circulation (e.g., Monismith 2007; Lowe and Falter 2015). As a result, the accurate prediction of wave setup on reefs is crucial for predicting a wide range of coastal hazards, such as coastal inundation and erosion resulting from large storms (Sheppard et al. 2005; Vetter et al. 2010; Storlazzi et al. 2011; Baldock et al. 2014).

Predictions of wave setup in the surfzone are typically based on partitioning wave forces (e.g., radiation stress gradients) into either pressure gradients (associated with wave setup) or bottom stresses through conservation of the mean (wave averaged) momentum (Longuet-Higgins and Stewart 1964). This theoretical balance is the foundation for most process-based nearshore hydrodynamic models. Wave forces in the surfzone are commonly approximated from linear wave theory, which assumes that waves are nonbreaking and of a near-constant form while propagating over an effectively flat bed (Longuet-Higgins and Stewart 1962, 1964). Despite the violation of these assumptions in the surfzone, on mildly sloping beaches radiation stress gradients derived from linear wave theory have often balanced observed cross-shore pressure gradients (Battjes and Stive 1985; Lentz and Raubenheimer 1999). However, the assumptions of linear wave theory are

Corresponding author address: Mark L. Buckley, School of Earth and Environment, University of Western Australia, 35 Stirling Highway, Crawley WA 6009, Australia.
E-mail: mark.buckley@uwa.edu.au

more questionable when applied to plunging waves on steep-slope beaches and reefs.

Despite the apparent misapplication of linear wave theory in these environments, models that predict wave forces using linear wave theory are still widely applied to steeply sloping reefs, with many reporting that even simple models can accurately reproduce setup observations (Gourlay 1996; Massel and Gourlay 2000; Becker et al. 2014; Buckley et al. 2014). However, in all of these studies the predicted setup was dependent on radiation stress gradients predicted using empirical or idealized models rather than wave observations. Hence, the good agreement reported may be owing to the tuning of coefficients that may not necessarily be physically meaningful. For example, Buckley et al. (2014) reported that tuning the Simulating Waves Nearshore (SWAN) model (Booij et al. 1999) to best reproduce the observed wave height decay across a laboratory reef profile often resulted in a reduction in the accuracy of wave setup predictions, which indicates a fundamental breakdown in the theoretical relationship between the predicted radiation stress gradients and the observed wave setup. In general, the lack of detailed observational data on steeply sloping reefs, particularly in the surfzone region, has made it difficult to rigorously evaluate the theory used to predict wave transformation and wave setup.

In this paper, we investigate the theoretical balance between cross-shore pressure and radiation stress gradients using high-resolution laboratory observations across a steeply sloping reef profile. In particular, we assess the ability of linear wave theory–derived radiation stress gradients approximated from observations to reproduce the observed setup and setdown responses. We also examine the contribution of a wave roller to the radiation stress (Svendsen 1984a; Reniers and Battjes 1997; Apotsos et al. 2007) as a means of including the high onshore directed surface velocities observed in the crests of breaking waves and associated turbulent bores (e.g., Govender et al. 2002). While this study specifically focuses on a representative fringing reef, our results are also relevant to understanding the mechanisms of wave setup generation by wave breaking on steep slopes more generally. The experiments were conducted in a 55-m-long flume (1:36 scale) with a 1:5 slope reef leading to a wide, shallow reef flat and sloping beach. The 16 cases were simulated, spanning a wide range of offshore wave heights and still water levels over a smooth bed and then repeated with scaled bottom roughness. In this paper, we focus on the smooth bed cases to assess the surfzone processes that control the mean water level variability; a follow-up paper (Buckley et al. 2015, manuscript submitted to *J. Phys. Oceanogr.*) will detail the effect of large bottom roughness.

2. Background

As our objective is to understand wave setup on a steep reef profile, we first outline the general theory and how it applies to our particular set of experiments.

a. Cross-shore mean momentum equation

For an alongshore uniform reef with normally incident waves, the wave-averaged, depth-integrated, cross-shore (x coordinate, positive shoreward from the reef crest) momentum equation can be written as (e.g., Mei 2005, p. 554)

$$\frac{\partial M_T}{\partial t} + \frac{\partial}{\partial x}\left[\frac{M_T^2}{\rho(h_0 + \overline{\eta})}\right] = -\rho g(h_0 + \overline{\eta})\frac{\partial \overline{\eta}}{\partial x}$$
$$-\frac{\partial S_{xx}}{\partial x} - \overline{\tau}_b\sqrt{1 + \left(\frac{\partial h_0}{\partial x}\right)^2}, \quad (1)$$

where the overbars denote time averaging over many wave periods; M_T is the depth-integrated and time-averaged Lagrangian mass flux; t is the time; ρ is the density; g is the gravitational acceleration; h_0 is the still water depth; $\overline{\eta}$ is the time-averaged deviation of the free-surface η from h_0; S_{xx} is the cross-shore component of the radiation stress tensor; and $\overline{\tau}_b$ is time-averaged bottom stress (see summary of notation in Table 1). In Eq. (1), we note that we have neglected two terms in the general form of the cross-shore momentum equation [see Mei 2005, p. 554, their Eq. (11.2.24)]. The first term neglected contains the time-averaged dynamic pressure at the bottom that is negligible compared to other terms included in Eq. (1), even on steep slopes [see Svendsen (2006), p. 536, for discussion]; the second term neglected contains a depth-integrated viscous stress term that is negligible relative to the other terms at sufficiently high Reynolds numbers [i.e., $O(10^3) \gg 1$ based on the wave orbital velocities in the present study; Mei 2005, p. 555]. Because of the design of the experiment, further simplifications of Eq. (1) are possible. For all cases considered here, the system was in steady state when averaged over many wave cycles (i.e., $\overline{\partial/\partial t} = 0$), and the shoreline was impermeable, such that the depth-integrated and time-averaged Lagrangian mass flux M_T was zero, thus eliminating all terms on the left-hand side (LHS) of Eq. (1). For the particular set of experiments described here, where the bottom was composed of smooth marine plywood to minimize the role of bottom roughness on setup, $\overline{\tau}_b$ was quantified to have a negligible effect on the closure of the mean momentum balance and the prediction of wave setup (see appendix A). Under these assumptions, Eq. (1) reduces to a dynamic balance between the radiation stress and pressure gradient terms:

TABLE 1. Notation.

Symbol	Definition	Unit
β	Reef slope	—
β_D	Wave-roller dissipation coefficient	—
$C_{\eta\eta}$, $C_{\eta\eta}^+$, $C_{\eta\eta}^-$	Wave power spectral density for the total, shoreward, and seaward components, respectively	$m^2\,Hz^{-1}$
c	Wave celerity	$m\,s^{-1}$
c_g	Wave group velocity	$m\,s^{-1}$
D_{br}	Wave energy dissipation rate due to breaking	$J\,m^{-2}\,s^{-1}$
E	Wave energy density	$J\,m^{-2}$
E_r	Kinetic energy of the wave roller	$J\,m^{-2}$
ξ_0	Deep-water surf similarity parameter	—
η	Free-surface deviation from h_0	m
$\overline{\eta}$	Time-averaged η (e.g., wave setup or setdown)	m
$\overline{\eta}_{pred}$	Predicted $\overline{\eta}$	m
$\overline{\eta}_r$	Time-averaged η on the reef flat	m
F, F^+, F^-	Wave energy flux for the total, shoreward, and seaward components, respectively	$J\,m^{-1}\,s^{-1}$
f	Frequency	Hz
f_p	Peak wave frequency	Hz
$\overline{f}_{SS}$, $\overline{f}_{IG}$	Mean frequency of the sea swell and infragravity waves, respectively	Hz
g	Acceleration due to gravity	$m\,s^{-2}$
H_{rms}	Rms wave height	m
$H_{rms,0}$	Deep-water rms wave height	m
h_0	Still water depth	m
$h_{0,r}$	Still water depth on the reef flat	m
KE, PE	Wave kinetic and potential energy, respectively	$J\,m^{-2}$
L_0	Deep-water wavelength	m
M_T	Depth- and time-averaged Lagrangian mass flux	$kg\,m^{-1}\,s^{-1}$
θ_η	Instantaneous free-surface inclination angle	°
θ_r	Wave-roller inclination angle	°
θ_w	Wave front inclination angle	°
P	Pressure	$N\,m^{-2}$
ρ	Density of water	$kg\,m^{-3}$
S_{xx}	Cross-shore component of the radiation stress tensor	$N\,m^{-1}$
$S_{xx,eff}$	Cross-shore component of the effective radiation stress	$N\,m^{-1}$
R_{xx}	Cross-shore component of the wave-roller radiation stress	$N\,m^{-1}$
T_p	Peak wave period	s
$\overline{\tau}_b$	Time-averaged (mean) bottom stress	$N\,m^{-2}$
$\overline{\tau}_t$	Time-averaged shear stress at the boundary of the wave and the wave roller	$N\,m^{-2}$
u, w	Velocity in the cross-shore and vertical directions, respectively	$m\,s^{-1}$
u', w'	Wave orbital velocities in the cross-shore and vertical directions, respectively	$m\,s^{-1}$

$$\underbrace{\frac{\partial S_{xx}}{\partial x}}_{\substack{\text{radiation stress} \\ \text{gradient}}} + \underbrace{\rho g(h_0 + \overline{\eta})\frac{\partial \overline{\eta}}{\partial x}}_{\substack{\text{pressure} \\ \text{gradient}}} = 0. \qquad (2)$$

$$S_{xx} = \underbrace{\overline{\int_{-h_0}^{\eta}(p + \rho u^2)\,dz}}_{\substack{\text{total} \\ \text{momentum flux}}} - \underbrace{\frac{1}{2}\rho g(h_0 + \overline{\eta})^2}_{\substack{\text{momentum flux} \\ \text{in the absence of waves}}}, \qquad (3)$$

The approach used to evaluate S_{xx} is summarized briefly in section 2b.

b. Radiation stresses

The cross-shore component of the radiation stress tensor S_{xx} can be defined as (e.g., Mei 2005, p. 554)

where z is the vertical coordinate (positive upward from h_0); $p\,(z)$ is the pressure; and $u\,(z)$ is defined as the deviation of the instantaneous velocity in the cross-shore direction from the depth- and time-averaged Lagrangian velocity. Typically when evaluating Eq. (3), all velocities other than wave orbital motion below $\overline{\eta}$ are neglected, the mean dynamic pressure below $\overline{\eta}$ is

approximated as $-\rho\overline{w'^2}$ (where w' is the vertical component of the wave orbital velocity), and the mean dynamic pressure above $\overline{\eta}$ is approximated as being hydrostatic (Longuet-Higgins and Stewart 1964; Mei 2005; Svendsen 2006). These assumptions are violated for breaking waves, particularly plunging breakers (Battjes 1988); however, these assumptions are required for use in both practical numerical and analytical models based on Eq. (2). These assumptions, along with linear wave theory expressions for η and the wave orbital velocities u' and w' (where u' is the wave orbital velocity in the cross-shore direction), yield

$$S_{xx} = E\left(2\frac{c_g}{c} - \frac{1}{2}\right), \qquad (4)$$

where E is the wave energy density (defined below), c_g is the wave group velocity, and c is the wave celerity. We note that Phillips (1977) derived an alternative S_{xx} to Eq. (4) based on a slightly different decomposition of the wave orbital and mean current velocities; however, as noted by Svendsen (2006) and Smith (2006), differences with Eq. (4) are generally small (on the order of the wave steepness to the fourth power; Svendsen 2006, p. 545).

From the experimental findings of Stive and Wind (1982) and Govender et al. (2002, 2009), as well as the three-dimensional finescale numerical simulations of Torres-Freyermuth et al. (2007), it appears that the largest source of uncertainty in the evaluation of S_{xx} for surfzone waves arises when evaluating $\rho\overline{u^2}$, specifically the contribution of velocities in the crest of breaking waves that is neglected in Eq. (4). Because of the dependence of S_{xx} on wave energy density E, it is useful to show the general form of E, which is composed of both potential energy (PE) and kinetic energy (KE) as (e.g., Dean and Dalrymple 1991, p. 97)

$$E = \underbrace{\frac{1}{2}\overline{\int_{-h_0}^{\eta}(\rho u'^2 + \rho w'^2)\,dz}}_{\text{KE}} + \underbrace{\frac{1}{2}\rho g\overline{(\eta - \overline{\eta})^2}}_{\text{PE}}. \quad (5)$$

In linear wave theory and other nonbreaking wave theories (e.g., cnoidal; Svendsen 2006, p. 420), both PE and KE are equal (e.g., Dean and Dalrymple 1991; Dean and Bender 2006), allowing E to be approximated from observations of sea surface variance alone [a measure of PE, per the final term of Eq. (5)]. However, the assumptions leading to PE = KE are explicitly violated under breaking waves (Svendsen 1984a; Battjes 1988). This can have important implications from the evaluation of radiation stress gradients in the surfzone. Wave-roller theory has been introduced to account for the

additional source of KE for breaking waves and therefore as an additional contribution to S_{xx}.

c. Wave-roller theory

Detailed particle image velocimetry (PIV) measurements of plunging waves (Govender et al. 2002) have shown much larger velocities in the crest region relative to nonbreaking waves. In the surfzone, this can locally result in KE > PE (e.g., Iwata and Tomita 1992). In wave-roller theory (Duncan 1981; Svendsen 1984a), some fraction of a breaking wave is partitioned into a wave roller with increased KE and shoreward mass flux. The wave roller is modeled independently of S_{xx} (similar to the approach of Apotsos et al. 2007) and does not contribute to η but simply modifies KE, providing an additional source of radiation stress R_{xx} according to (Svendsen 1984a)

$$R_{xx} = 2E_r, \qquad (6)$$

where E_r is the kinetic energy of the wave roller modeled using an approximate energy balance following Stive and De Vriend (1994):

$$\frac{\partial}{\partial x}(2E_r c) = D_{\text{br}} - \overline{\tau}_t c, \qquad (7)$$

where D_{br} is wave-breaking dissipation, and $\overline{\tau}_t$ is the mean shear stress at the boundary between the turbulent wave roller and the underlying organized wave motion. Conceptually, wave-roller theory implies that PE is initially transferred to KE during wave breaking and KE is dissipated via shear stresses (i.e., momentum exchange). The mean shear stress $\overline{\tau}_t$ is approximated as (Dally and Brown 1995)

$$\overline{\tau}_t = \frac{2gE_r}{c^2}\beta_D, \qquad (8)$$

where $\beta_D = \sin\theta_r\cos\theta_r$ is a dissipation coefficient that depends on the angle θ_r of inclination of the boundary between the turbulent wave roller and the underlying organized wave motion (Dally and Brown 1995). This dissipation mechanism implies a slowly changing wave shape, that is, a quasi-steady breaking process (Dally and Brown 1995) that may not develop in the initial overturning stage of plunging wave breaking. However, the plunging distance, which is generally less than the breaking wave height (Bowen et al. 1968; Grilli et al. 1997), is very small relative to the total surfzone width such that steady bores are usually observed to develop even for initially plunging waves (Okayasu et al. 1986; Bonmarin 1989). Furthermore, despite the decrease in PE in the plunging region, pressure gradients have been
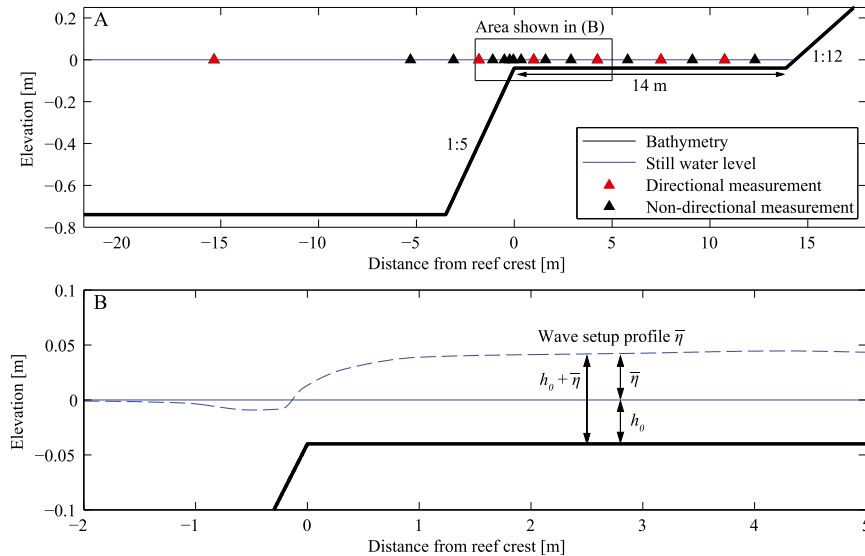
FIG. 1. (a) Schematic of the fringing reef showing the reef slope (1:5), reef flat length (14 m; ~500-m field scale), beach slope (1:12), and instrument locations. Directional measurement sites have collocated water level and velocity measurements, whereas other nondirectional sites have only water level measurements. Many of the subsequent figures will focus on the area in the vicinity of the reef crest (black box), where radiation stress gradients and pressure gradients were the largest. (b) An example of the wave setup profile $\overline{\eta}$ in the vicinity of the reef crest for run 4, defining the still water depth h_0 and the total water depth $h_0 + \overline{\eta}$.

found to be small (e.g., Bowen et al. 1968), indicating that this region is less important for setup generation than the decrease in PE would suggest (Svendsen 1984a). Thus, with turbulent bores propagating over much of the total surfzone region, the basic assumptions of the wave-roller dissipation model can still hold, although we evaluate this in detail using the observations below (section 4).

3. Methods

a. Experimental setup

Experiments were performed in a 55-m-long wave flume (Eastern Scheldt flume) at Deltares, the Netherlands (Fig. 1). The reef profile was constructed from marine plywood and had a 1:5 reef slope, a 14-m horizontal reef flat, and a 1:12 beach (Fig. 1). Based on the 1:36 geometric scaling assumed in this study, this represents a 500-m-long reef flat in field (prototype) scale that is comparable to the global median coral reef flat length of 450 m reported by Falter et al. (2013). Published reef slopes vary from being relatively mild (e.g., ~1:60 Kaneohe Bay, Hawaii; Lowe et al. 2009) to nearly vertical (e.g., Gourlay 1996). A 1:5 slope was chosen to be representative of the steeper range of natural reef slopes yet still well within the typical range.

Waves were generated with a piston-type wave maker with second-order wave generation and active reflection compensation of any seaward-propagating waves reflected back to the wave maker from the reef slope and beach (van Dongeren et al. 2002). Irregular waves were generated with a TMA-type spectrum (Bouws et al. 1985). A total of 16 runs were conducted with varying still water depths on the reef flat $h_{0,r}$ and offshore wave conditions (Table 2). Wave periods, and time scales in general, are scaled by matching the Froude number, which ensures that gravity forces are correctly scaled and yields a time scaling factor of 1:6. The surf similarity parameter ($\xi_0 = \beta/\sqrt{H_{\mathrm{rms},0}/L_0}$) can provide an estimate of how waves should break on the reef slope (Battjes 1974), where $\beta = \frac{1}{5}$ is the reef slope, $H_{\mathrm{rms},0}$ is the deep-water root-mean-square (rms) wave height $H_{\mathrm{rms}} = \sqrt{8(\eta - \overline{\eta})^2}$, and L_0 is the deep-water wavelength. Waves in this study were typically plunging, as predicted by ξ_0 (plunging regime of $0.5 \leq \xi_0 \leq 3.3$) (Table 2; Battjes 1974).

Water levels were measured using resistance wave gauges (GHM, Deltares) sampling synchronously at 40 Hz at 17 locations, with the highest density of measurements in the surfzone region near the reef crest at $x = 0$ m (Fig. 1). Horizontal velocities were also measured synchronously at 40 Hz using programmable electromagnetic current sensors (P-EMS, Deltares) at

TABLE 2. Simulated wave and water level conditions including the deep water rms wave height $H_{rms,0}$, the peak period T_p, the still water depth on the reef flat $h_{0,r}$, the deep-water wave steepness $H_{rms,0}/L_0$, and the deep-water surf similarity parameter ξ_0. Parameter values are given for both the laboratory scale (1:36 geometric scaling and 1:6 scaling of time) and the equivalent field scale.

	Laboratory scale			Field scale				
Run	$H_{rms,0}$ (m)	T_p (s)	$h_{0,r}$ (m)	$H_{rms,0}$ (m)	T_p (s)	$h_{0,r}$ (m)	$H_{rms,0}/L_0$ (—)	ξ_0 (—)
1	0.03	2.26	0.04	1.1	13.6	1.4	0.004	3.3
2	0.06	2.26	0.04	2.2	13.6	1.4	0.007	2.4
3	0.09	2.26	0.04	3.2	13.6	1.4	0.011	1.9
4	0.12	2.26	0.04	4.3	13.6	1.4	0.015	1.7
5	0.14	2.26	0.04	5.0	13.6	1.4	0.018	1.5
6	0.17	2.26	0.04	6.1	13.6	1.4	0.021	1.4
7	0.06	1.31	0.04	2.2	7.9	1.4	0.021	1.4
8	0.06	3.20	0.04	2.2	19.2	1.4	0.004	3.4
9	0.06	2.26	0.00	2.2	13.6	0.0	0.009	2.2
10	0.06	2.26	0.02	2.2	13.6	0.7	0.009	2.2
11	0.06	2.26	0.06	2.2	13.6	2.2	0.008	2.3
12	0.06	2.26	0.09	2.2	13.6	3.2	0.008	2.3
13	0.12	2.26	0.00	4.3	13.6	0.0	0.015	1.7
14	0.12	2.26	0.02	4.3	13.6	0.7	0.015	1.7
15	0.12	2.26	0.06	4.3	13.6	2.2	0.015	1.7
16	0.12	2.26	0.09	4.3	13.6	3.2	0.015	1.6

six locations collocated with wave gauges (Fig. 1). On the reef flat and reef slope, the GHMs and P-EMSs were recessed into the bed in order to be able to sample in the shallow depths (Eslami Arab et al. 2012); the P-EMSs at these locations sampled velocity at a height 2 cm above the bed, with the sample volume extending 0.5 cm above the sensor. P-EMSs at other offshore locations sampled at approximately the middle of the water column.

b. Evaluation of the mean momentum equation

Wave motions in the flume can in general be composed of both shoreward- and seaward-propagating components. As the evaluation of S_{xx} gradients is sensitive to the direction of wave propagation, a directional wave analysis was performed using a frequency domain algorithm (appendix B), which required synchronous water level and velocity time series. This analysis yielded predictions of the shoreward-propagating ($^+$) and seaward-propagating ($^-$) components of the instantaneous water level signal at instrument locations with collocated water level and velocity measurements (i.e., "directional" sites); other sites with only water level measurements are referred to as "nondirectional" sites (Fig. 1). Wave spectra $C_{\eta\eta}$, as well as shoreward $C_{\eta\eta}^+$ and seaward $C_{\eta\eta}^-$ components (at directional sites), were computed from water level measurements using Welch's modified periodogram method with a Hanning window and a segment length of 2^{14} samples (410 s; 41 min in field scale). From $C_{\eta\eta}^+$ the radiation stress S_{xx} for a frequency spread (i.e., random) wave field can be approximated using linear wave theory as (Battjes 1972)

$$S_{xx} = \int \rho g C_{\eta\eta}^+ \left(2\frac{c_g}{c} - \frac{1}{2}\right) df, \tag{9}$$

where $c_g(f)$ and $c(f)$ are the group and phase velocities, respectively, at frequency f. Equation (9) is the equivalent spectral form of Eq. (4). As the evaluation of Eq. (9) requires directional information not available at all locations, directional information was interpolated to the nondirectional sites using linear wave energy flux (i.e., $F = c_g E$) of which the shoreward component of F^+ is related to S_{xx} as

$$S_{xx} = \frac{F^+}{c_g}\left(2\frac{c_g}{c} - \frac{1}{2}\right). \tag{10}$$

The nondirectional linear wave energy flux F was calculated at all instrument sites from $C_{\eta\eta}$ as

$$F = \int c_g \rho g C_{\eta\eta}\, df. \tag{11}$$

The definition $F^+ = F - F^-$ was used to evaluate F^+ from the computed F [Eq. (11)] and the seaward component F^-, which was computed at directional sites [via Eq. (11) using $C_{\eta\eta}^-$ rather than $C_{\eta\eta}$] and then linearly interpolated to adjacent nondirectional sites. The seaward component F^- was used for the interpolation as it is independent of wave shoaling and less dependent on breaking dissipation than F^+. Furthermore, in the evaluation of Eqs. (10) and (11), we distinguished between sea swell (SS) defined as $f \geq f_p/2$, where f_p is the peak forcing frequency of each wave case, and

infragravity (IG) defined as $0.025 \leq f < f_p/2$ components. This allowed S_{xx} to be evaluated at every instrument using Eq. (10) as

$$
\begin{aligned}
S_{xx} &= S_{xx,\text{SS}} + S_{xx,\text{IG}} \\
&= \frac{F_{\text{SS}}^+}{c_g(\bar{f}_{\text{SS}})} \left[2 \frac{c_g(\bar{f}_{\text{SS}})}{c(\bar{f}_{\text{SS}})} - \frac{1}{2} \right] + \frac{F_{\text{IG}}^+}{c_g(\bar{f}_{\text{IG}})} \left[2 \frac{c_g(\bar{f}_{\text{IG}})}{c(\bar{f}_{\text{IG}})} - \frac{1}{2} \right],
\end{aligned}
$$

(12)

where $S_{xx,\text{SS}}$ and $S_{xx,\text{IG}}$ are the SS and IG components of radiation stress, respectively; $\bar{f}_{\text{SS}}$ and $\bar{f}_{\text{IG}}$ are the mean frequencies for the SS and IG waves, respectively; and F_{SS}^+ and F_{IG}^+ are the SS and IG components of the shoreward wave energy flux, respectively. The use of mean frequencies in Eq. (12) [vs computing S_{xx} spectrally from Eq. (9)] introduces the assumption that SS and IG components were narrowbanded [see Feddersen (2004) for discussion]; however, comparisons with the full spectral integration Eq. (9) at directional sites showed minimal differences in the values of S_{xx} estimated from Eq. (12).

The cross-shore gradients required to estimate the pressure and radiation stress gradients were evaluated by interpolating the observations of $\bar{\eta}$, $\bar{f}_{\text{SS}}$, $\bar{f}_{\text{IG}}$, F_{SS}^+, and F_{IG}^+, using a shape-preserving piecewise cubic algorithm onto a uniform 0.01-m grid extending from offshore ($x = -2.0$ m) to near the shoreline ($x = 14$ m). Over this domain, the cross-shore distance between wave gauges varied from 0.19 m in the surfzone to 1.7 m on the reef flat (Fig. 1). This spacing is equivalent to as low as ~1/40 of the incident wavelength in the surfzone to ~¼ on the reef flat. Cross-shore gradients were computed using central differencing and cross-shore integration was done using trapezoidal integration. At each grid location, S_{xx} was evaluated from $\bar{f}_{\text{SS}}$, $\bar{f}_{\text{IG}}$, F_{SS}^+, and F_{IG}^+ using Eq. (12). Similarly, R_{xx} was evaluated from $\bar{f}_{\text{SS}}$, F_{SS}^+, and F_{IG}^+ using Eqs. (6)–(8) and a simple forward integration scheme. The growth term in the wave-roller model Eq. (7) is equivalent to the breaking wave energy dissipation, calculated as $D_{\text{br}} = -\partial(F_{\text{SS}}^+ + F_{\text{IG}}^+)/\partial x$. As the wave roller is predominantly associated with SS waves, wave celerity in Eqs. (7) and (8) was taken as $c(\bar{f}_{\text{SS}})$. In section 4c, we evaluate how the results respond to different values of β_D (related to the wave-roller slope) in the wave-roller dissipation formula equation (8) and also compare these values with wave gauge estimates of the wave front inclination angle. In this study, $\beta_D = 0.19$ was found to be optimum (see section 4c) and is used throughout the paper.

The cross-shore mean momentum balance Eq. (2) was rearranged and integrated in the cross-shore direction to give a "prediction" of the setup $\bar{\eta}_{\text{pred}}$ across the reef as (e.g., Raubenheimer et al. 2001)

$$
\bar{\eta}_{\text{pred}} = -\int_{x_0}^{x} \frac{1}{\rho g(h_0 + \bar{\eta}_{\text{pred}})} \frac{\partial(S_{xx} + R_{xx})}{\partial x} dx + \bar{\eta}(x_0), \quad (13)
$$

where the integration is initialized at a seaward boundary x_0 ($x_0 = -2$ m in Fig. 1) with the observed time-averaged water level $\bar{\eta}(x_0)$ [$\bar{\eta}(x_0) = 0$ if x_0 is in deep water] and evaluated iteratively. Equation (13) was evaluated with S_{xx} and R_{xx} approximated from the interpolated observations and used to evaluate the skill of S_{xx} and R_{xx} to reproduce observations of $\bar{\eta}$. Last, Eq. (2) was also used to provide an estimate of the radiation stress $S_{xx,\text{eff}}$ required to balance the observed $\bar{\eta}$ as (e.g., Svendsen and Putrevu 1993)

$$
S_{xx,\text{eff}} = -\int_{x_0}^{x} \rho g(h_0 + \bar{\eta}) \frac{\partial \bar{\eta}}{\partial x} dx + S_{xx}(x_0) + R_{xx}(x_0),
$$

(14)

where $S_{xx}(x_0)$ and $R_{xx}(x_0)$ are the initial values of S_{xx} and R_{xx}, respectively, at the offshore boundary of integration [$R_{xx}(x_0) = 0$ if x_0 is outside of the surfzone].

c. Uncertainty estimation

Measurement uncertainties for the GHM and P-EMS are small; calibration confirmed a maximum error of $\pm 0.5\%$ of the measured range for water levels and ± 0.01 m s^{-1} $\pm 1\%$ of measured values for velocity (Deltares). At surfzone locations these instruments can be expected to be less accurate due to aeration of the water column during wave breaking (e.g., Stive and Wind 1982). By comparing similar wave gauges with video analysis, Stive and Wind (1982) give a conservative estimate of the uncertainty due to aeration effects of $\pm 1\%$ of the measured range for time-averaged water levels and $\pm 2.5\%$ for the measurement of wave heights. Combining uncertainties due to calibration and aeration effects gave $\pm \sim 0.5\%$ outside of the surfzone and $\pm \sim 1.5\%$ within the surfzone of the measured range for time-averaged water levels. Likewise, the uncertainties for parameters proportional to wave height squared (i.e., wave energy and radiation stress) were $\pm \sim 2\%$ outside of the surfzone and $\pm \sim 7\%$ inside the surfzone. The effect of these uncertainties on the cross-shore integration of Eqs. (13) and (14) was assessed by performing 100 Monte Carlo simulations, where uncertainties were modeled as having zero-mean Gaussian random distributions with a standard deviation based on the uncertainty. Velocity measurements were only used for estimating the effect of wave reflection (appendix B), which we show below in section 4a has a minor effect on the calculated radiation stress gradients and as such is not considered a large factor in the uncertainty estimates.
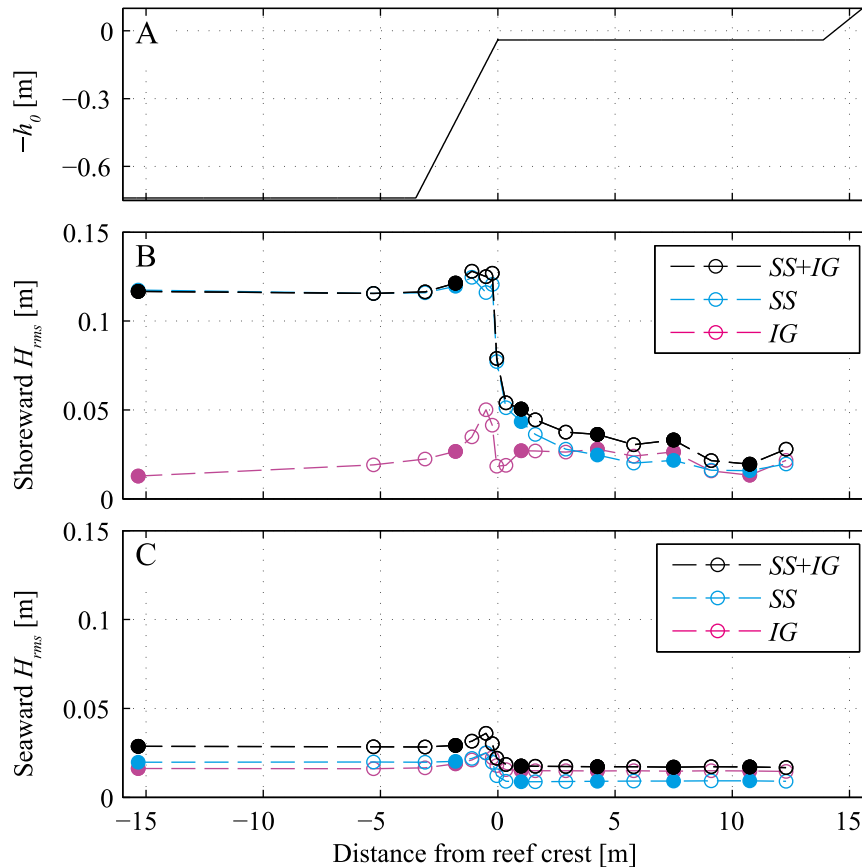
FIG. 2. (a) The bathymetric profile h_0, (b) the shoreward-propagating component of rms wave height, and (c) the seaward-propagating component of rms wave height are shown for run 4. In each subplot the total (SS + IG), SS, and IG components are shown. In (b) and (c), closed circles are direct estimates of the shoreward and seaward components (i.e., locations with water level and velocity data), while open circles rely on interpolation of the seaward component as described in section 3b.

4. Results

a. Wave transformation

To illustrate the general features of wave transformation across the reef, we initially focus on results from run 4 with moderately large wave conditions ($H_{\mathrm{rms},0} = 0.12$ m, $T_p = 2.26$ s or equivalent to $H_{\mathrm{rms},0} = 4.3$ m, $T_p = 13.6$ s in field scale) with an intermediate still water depth ($h_r = 0.04$ m or $h_r = 1.4$ m in field scale; Fig. 2). This run is used to highlight many of the common trends observed within the full array of runs, which differed primarily in terms of the magnitude of the wave height and setup responses. Figure 2 shows a rapid reduction in SS rms wave height in the vicinity of the reef crest ($x = 0$ m) associated with depth-induced breaking. A video sequence of a typical wave plunging near the reef crest is also depicted in Fig. 3. A comparison with the shoreward component of the total wave height (SS + IG) shows that the IG waves

contributed little to the total surfzone wave height gradients, despite SS and IG rms wave heights being comparable on the reef flat (Fig. 2b). Wave reflection was small relative to wave-breaking dissipation (Fig. 2c), with only 3% of SS and 6% of the total (SS + IG) wave energy flux reflected for run 4 (values were of similar magnitude for the other runs; appendix B).

b. Radiation stresses, momentum balances, and setup/setdown

The shoreward-propagating SS and IG wave energy fluxes F^+ (Fig. 4b) were used to evaluate the radiation stress from linear wave theory S_{xx} via Eq. (12) and a contribution from the wave-roller R_{xx} via Eq. (6) (Fig. 4c). These radiation stresses were used to predict wave setup profile via Eq. (13) and compared with the observations (Fig. 4d). The inclusion of the wave roller improved the predictions of both setdown and setup by
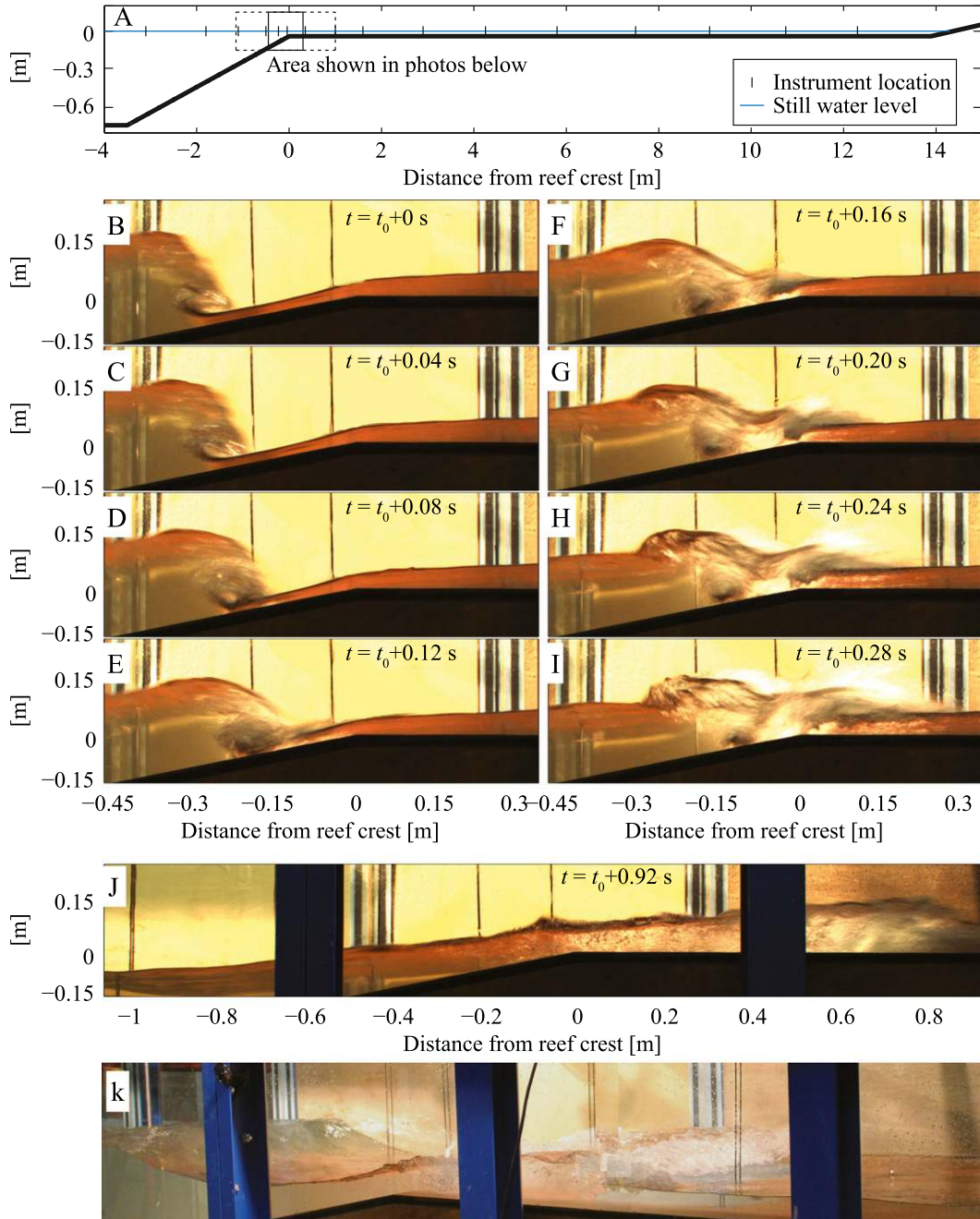
FIG. 3. (b)–(i) Wave plunging sequence taken during run 4 in the immediate vicinity of the reef crest [solid box in (a)]. In (b)–(j), the notation t_0 denotes the start of the breaking sequence with a frame rate of ~25 Hz. The area of the photos is where the most intense wave breaking occurred and only covers a small portion of the total reef slope and reef flat shown in (a). (j) Larger area [(a), dashed box] showing the development of a steady bore at $x = 0.8$ m propagating shoreward on the reef flat. (k) Oblique photograph showing a bore on the reef flat and a wave steepening on the reef slope.

introducing a spatial delay between the dissipation of PE and the associated radiation stress ($S_{xx} + R_{xx}$) gradients [Fig. 4d]. The improved agreement was most noticeable on the seaward portion of the reef flat where

$\overline{\eta}$ and $\overline{\eta}_{\mathrm{pred}}$ calculated from $S_{xx} + R_{xx}$ gradients continue to increase despite $\overline{\eta}_{\mathrm{pred}}$ calculated without the wave roller reaching an approximate maximum at $x = 0.35$ m [Fig. 4d]. However, comparing $S_{xx} + R_{xx}$ with $S_{xx,\mathrm{eff}}$
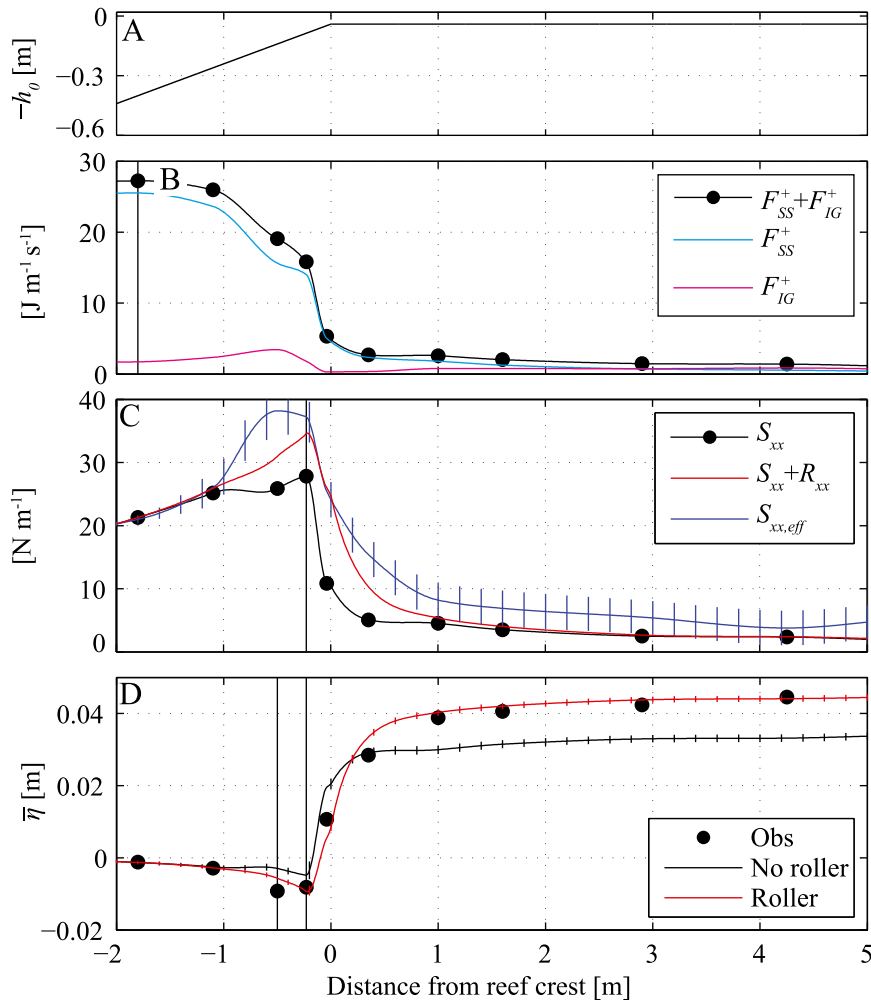
FIG. 4. (a) The bathymetric profile h_0 and (b) the shoreward-propagating components of the wave energy flux F^+ are shown in the vicinity of the reef crest for run 4 (black box in Fig. 1a). (c) The radiation stresses S_{xx} and R_{xx} are the contribution from linear wave theory [Eq. (12)] and the wave-roller [Eq. (6)], respectively. The effective radiation stress $S_{xx,\mathrm{eff}}$ is the radiation stress needed to close the mean momentum equation via Eq. (14). (d) Radiation stresses S_{xx} (no roller) and $S_{xx} + R_{xx}$ (roller) were used to evaluate $\overline{\eta}_{\mathrm{pred}}$ via Eq. (13) and compared with observations (Obs). Vertical error bars are given for $S_{xx,\mathrm{eff}}$ and $\overline{\eta}_{\mathrm{pred}}$ (see section 3c). Vertical black lines give: (b) the start of wave dissipation and hence wave-roller growth, (c) the maximum S_{xx}, and (d) the region of maximum setdown.

[i.e., the latter reflecting the S_{xx} needed to produce the observed setup per Eq. (14)] shows that in order to match the observed wave setup, $S_{xx} + R_{xx}$ would still need to be slightly larger during the initial wave setdown and decay slightly more slowly shoreward of the reef crest (Fig. 4c). However, these discrepancies only represent a very minor correction of 3%–5% to the wave setup predicted from $S_{xx} + R_{xx}$ on the reef flat (Fig. 4d). Figure 5 provides two additional examples of S_{xx} and $\overline{\eta}$ profiles for runs 13 and 16 (also discussed further below); these runs had the same incident wave forcing as run 4 but with $h_{0,r}$ of 0 and 0.09 m, respectively.

Of particular interest is the setup on the reef flat that establishes the water level that will interact with a shoreline. The setup was relatively constant across the majority of the reef flat ($x > 4$ m; Figs. 4d, 5b, 5d) for all 16 runs, allowing us to define a mean reef setup $\overline{\eta}_r$ between $x = 4$ and 10 m. To assess how offshore wave properties and still water levels influenced $\overline{\eta}_r$, we compare $\overline{\eta}_r$ with the cross-shore integrated radiation stress gradient:

$$-\int_{x_0}^{x} \frac{\partial(S_{xx} + R_{xx})}{\partial x} dx \equiv -\Delta(S_{xx} + R_{xx}), \quad (15)$$
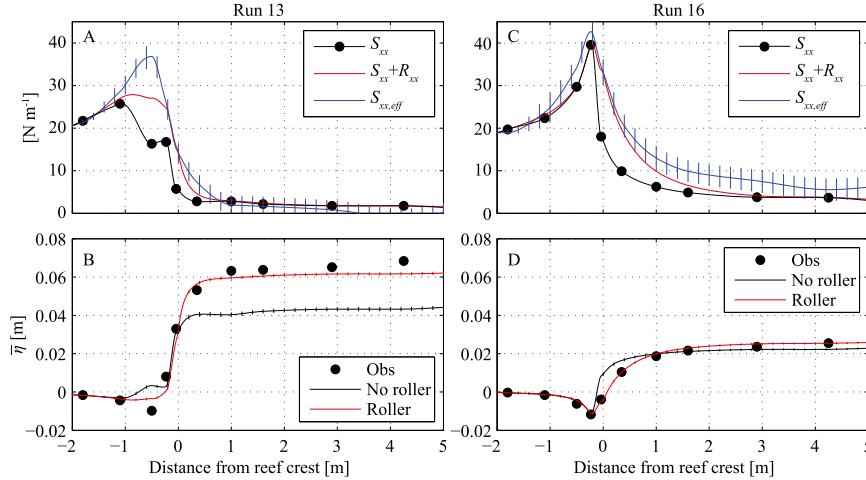
FIG. 5. (a),(c) Radiation stresses S_{xx} (no roller) and $S_{xx} + R_{xx}$ (roller) were used to evaluate (b),(d) $\overline{\eta}_{\text{pred}}$ via Eq. (13) and compared with observations in the vicinity of the reef crest for (left) run 13 and (right) run 16. Vertical error bars are given for $S_{xx,\text{eff}}$ and $\overline{\eta}_{\text{pred}}$ (see section 3c).

where the bounds of integration were taken from seaward of the break point ($x = -2$ m) to a point on the reef flat ($x = 4$ m) shoreward of the surfzone where $\overline{\eta}$ becomes relatively constant (i.e., $\overline{\eta} \approx \overline{\eta}_r$). As these bounds of integration are both outside of the surfzone, this evaluation is independent of whether the wave roller is considered or not [i.e., $-\Delta(S_{xx} + R_{xx}) = -\Delta S_{xx}$ depends only on the endpoint values of S_{xx}]. For runs with constant T_p and $h_{0,r}$ (runs 1–6; Table 2), $\overline{\eta}_r$ displays a sublinear dependence on $-\Delta S_{xx}$ (Fig. 6). This is consistent with Eq. (13), where $\overline{\eta}$ becomes an increasing proportion of $h_0 + \overline{\eta}$ as $-\Delta S_{xx}$ increases. For a given range of $-\Delta S_{xx}$, variations in $h_{0,r}$ had a large influence on $\overline{\eta}_r$ (Fig. 6; both runs 2, 8–12 and 4, 13–16), with decreases in $h_{0,r}$ causing $\overline{\eta}_r$ to increase. For example $\overline{\eta}_r$ was $\sim$2.5 times greater for run 13 ($h_{0,r} = 0$ m) than run 16 ($h_{0,r} = 0.09$ m) despite having a comparable $-\Delta S_{xx}$ (Figs. 5, 6).

If the cross-shore integrated pressure gradient $[\int \rho g(h_0 + \overline{\eta})(\partial \overline{\eta}/\partial x)\,dx]$ is instead considered (rather than $\overline{\eta}_r$) (Fig. 7), this mostly collapses the trends observed in Fig. 6. Equation (2) predicts a 1:1 relationship should occur between the cross-shore integrated pressure gradient and $-\Delta S_{xx}$. Our results indicate that the trend is mostly 1:1, with nearly all runs falling within the uncertainty of the measurements (Fig. 7).

Cross-shore integration over the entire surfzone, as done in Fig. 7, incorporates the cumulative effects of processes that contribute to both setdown ($\partial \overline{\eta}/\partial x < 0$) and setup ($\partial \overline{\eta}/\partial x > 0$). To investigate the dynamics of setdown and setup in more detail, we cross-shore integrated Eq. (2) over two separate regions (Fig. 8): 1) a region of setdown from offshore ($x = -2$ m) to a

"transition point," defined as the point of maximum setdown (usually $x = -0.5$ to -0.2 m), and 2) a region of setup from the transition point to $x = 4$ m, where $\overline{\eta}$ becomes relatively constant. We note that this transition point of maximum setdown is also used by Svendsen (1984a) to define the transition between the "outer surfzone" and the "inner surfzone," where the outer surfzone is characterized by rapid wave transformation (but comparatively small pressure gradients) and the inner surfzone is characterized by the development of steady turbulent bores and rapid wave setup generation.
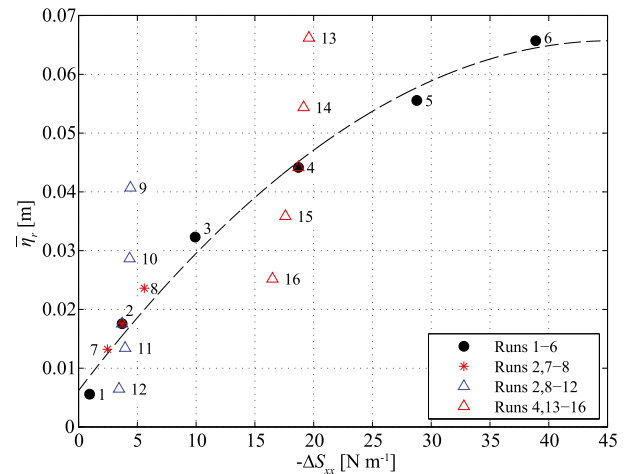

FIG. 6. Variation of $\overline{\eta}_r$ with $-\Delta S_{xx}$ calculated from offshore to $x = 4$ m. Symbols denote runs with shared conditions and a single variable changed. A quadratic, least squares trend line is given of runs 1–6. Numbers adjacent to symbols denote the run number (refer to Table 2).
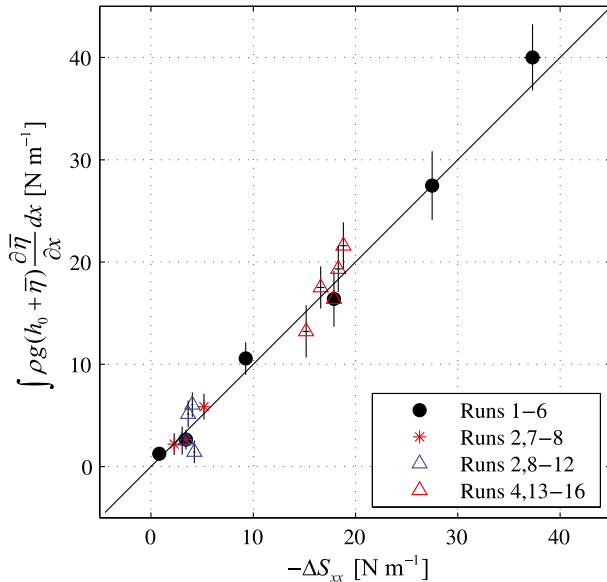
FIG. 7. Variation of the cross-shore integrated ($x = -2$ to 4 m) pressure gradient with the cross-shore integrated radiation stress gradient [$-\Delta S_{xx}$; Eq. (15)] for the 16 wave and water level conditions. As the cross-shore integration spans the entire surfzone, this analysis is independent of the wave roller [i.e., $-\Delta(S_{xx} + R_{xx}) = -\Delta S_{xx}$]. The mean momentum equation [Eq. (2)] predicts a 1:1 relationship (black line) should exist. Vertical and horizontal (typically not visible) error bars show the uncertainties due to instrument accuracy (see section 3c).

As the transition point is often within the surfzone (defined by $D_{br} > 0$), $-\Delta(S_{xx} + R_{xx})$ is sensitive to the inclusion of the wave roller. For the setdown region (Fig. 8a), 11 of the 16 runs had much more negative cross-shore integrated pressure gradients than $-\Delta S_{xx}$ would predict via Eq. (2). This is consistent with the underprediction of setdown shown for runs 4 and 13 without the wave roller (Figs. 4d, 5b). Conversely, for the wave setup region (Fig. 8c), 10 of the 16 runs had larger cross-shore integrated pressure gradients than $-\Delta S_{xx}$, consistent with the underprediction of setup shown for runs 4 and 13 (Figs. 4d, 5b). Together with Eq. (2), these results suggest that the actual radiation stresses at the transition point were larger than calculated from observations via the linear wave theory approximation of radiation stress [Eq. (12)]. However, as seen in the prediction of setdown/setup profiles (Figs. 4d, 5b,d), including the contribution from the wave-roller R_{xx} [i.e., $-\Delta(S_{xx} + R_{xx})$ rather than $-\Delta S_{xx}$] substantially improved the agreement between the cross-shore integrated radiation stress and pressure gradients over both the setdown (Fig. 8b) and setup regions (Fig. 8d).

Because of these momentum balances, both wave setdown and setup were underpredicted for many runs

using S_{xx} alone (Fig. 9). For setdown, 8 of the 16 runs were underpredicted by an average of 49%; this underprediction was approximately halved (26%) with the inclusion of the wave roller (i.e., $S_{xx} + R_{xx}$). For setup, 12 of the 16 runs were underpredicted by an average of 21%; inclusion of the wave roller reduced the error to just 3%. The underprediction of setdown and setup, without the inclusion of the wave roller, was most pronounced for runs with larger wave heights and lower still water levels (i.e., cases with the greatest setdown and setup). These runs also had relatively low ξ_0 values due to the dependence on offshore wave height. For the full array of runs, the improvement found by including the wave roller was substantial for $\xi_0 < 2.3$; however, for the five runs with $\xi_0 \geq 2.3$ (Table 2), both the setdown and setup predictions were not significantly improved with inclusion of the wave roller. Run 8 (Figs. 9a,b; cyan circle) was the most extreme example with $\xi_0 = 3.4$ (Table 2), for which a surging breaker type is predicted (Battjes 1974). For this particular run, the predicted wave setdown was considerably larger than observed (Fig. 9a). Run 8 was also the only run where the predicted setup was substantially less accurate when including the wave roller (Fig. 9b).

c. Parameterization of the wave-roller model

We investigate how the accuracy of the setup prediction $\overline{\eta}_{\text{pred}}$ depends on β_D via Eq. (8), the sole parameter in the wave-roller model. As described in section 3b, a single optimum value of $\beta_D = 0.19$ had been applied consistently across all runs, which was based on assessing the sensitivity of the wave-roller model by varying β_D from 0 to 0.5 in increments of 0.01 (equivalent to varying θ_r from 0° to 45°; recall $\beta_D = \sin\theta_r\cos\theta_r$), which is now described here. To assess how β_D influences the predicted the setdown/setup profiles via Eq. (13), for each run we evaluate the relative rms error ϵ_{rms} defined as

$$\epsilon_{\text{rms}} = \sqrt{\frac{1}{N}\sum\left(\frac{\overline{\eta}_{i,\text{pred}}}{\overline{\eta}_r} - \frac{\overline{\eta}_{i,\text{obs}}}{\overline{\eta}_r}\right)^2}, \qquad (16)$$

where N is the total number of measurement sites and i denotes an individual measurement location. For most runs (Fig. 10), using $\beta_D < 0.10$ results in high error (relative to other β_D values), which is equivalent to the mild wave-roller inclination angle of $\theta_r < 6°$. However, ϵ_{rms} is generally low when $\beta_D > 0.10$ (Fig. 10). For almost all runs, the optimum β_D fell between 0.1 and 0.3. Runs 1, 8, and 12, where both $\overline{\eta}_r$ was small (Fig. 6) and where $\xi_0 \geq 2.3$ (Table 2), are exceptions with lower
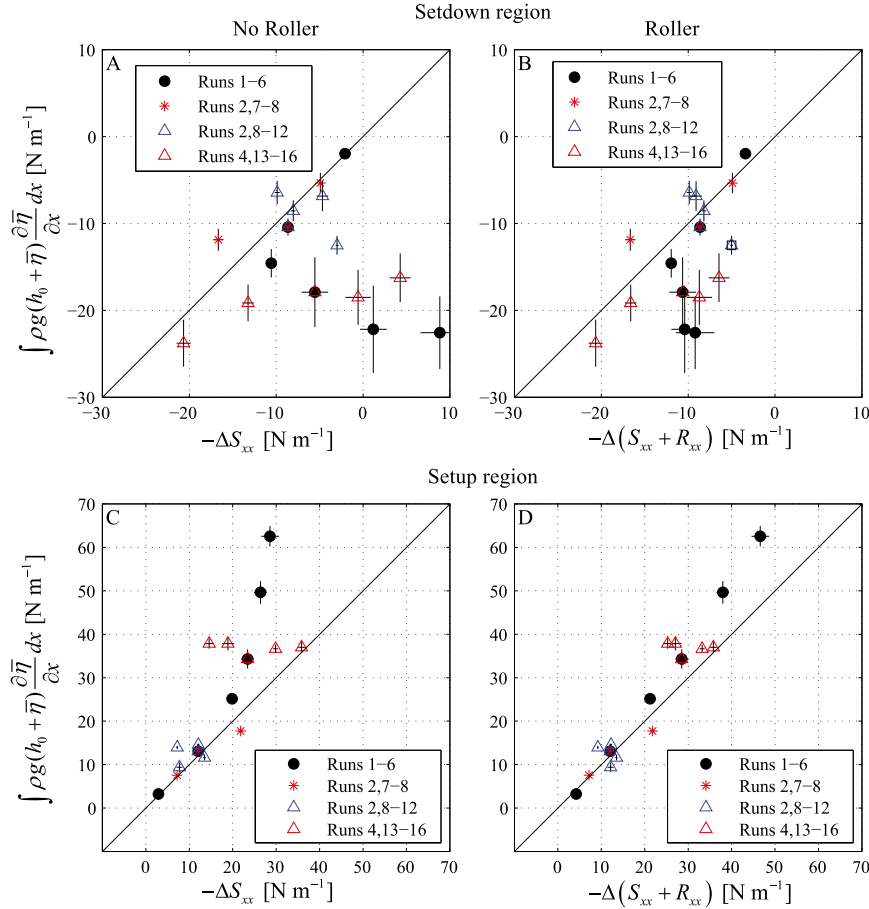
FIG. 8. Variation of the pressure and radiation stress gradients cross-shore integrated (a),(b) from offshore ($x = -2$ m) to maximum setdown and (c),(d) from maximum setdown to shoreward of the surfzone ($x = 4$ m). The radiation stress gradients were evaluated (left) without ($-\Delta S_{xx}$) and (right) with $[-\Delta(S_{xx} + R_{xx})]$ the wave roller. The mean momentum equation Eq. (2) predicts a 1:1 relationship (black lines) should exist for any integration region. Note the factor of 2 change in the axis scale between (a),(b) and (c),(d). Vertical and horizontal (typically not visible) error bars show the uncertainties due to instrument accuracy (see section 3c).

values of β_D improving the results. However, as noted previously, these were among the only runs where the setup predictions were not improved by including the wave roller. In addition, run 10 had a very high optimum β_D of 0.4; however, as seen for several other runs (notably run 2–4), run 10 was generally insensitive to $\beta_D >$ 0.10. Overall, the mean optimum β_D for all runs was 0.19 ($\theta_r = 11°$), approximately twice the $\beta_D = 0.1$ Reniers and Battjes (1997) reported to be optimum for spilling waves (with $\xi_0 = 0.2$–0.4 for waves breaking on their 1:20 beach slope).

Heuristically, we could expect there to be some physical relationship between the wave-roller inclination angle θ_r within the wave-roller dissipation model [Eq. (8)] and the wave front inclination angle θ_w in the surfzone that generally increases with breaker type from spilling to

plunging (Battjes 1974). To investigate this, we obtained an estimate of θ_w from the water level time series in the surfzone and compared these values with the optimum θ_r from Fig. 10. The instantaneous free-surface inclination angle θ_η was estimated from the time rate of change of η from the water level time series based on the kinematic surface boundary condition as

$$\theta_\eta(x,t) = \tan^{-1}\left(\frac{\partial \eta}{\partial x}\right) \approx \tan^{-1}\left[\frac{1}{c(\bar{f}_{SS})}\frac{\partial \eta}{\partial t}\right]. \quad (17)$$

For the calculation of individual trough-to-crest wave front inclination angles, individual waves were isolated using a zero-crossing analysis, and the rms value of the individual trough-to-crest wave front inclination angles were taken as θ_w. Figure 11 shows the
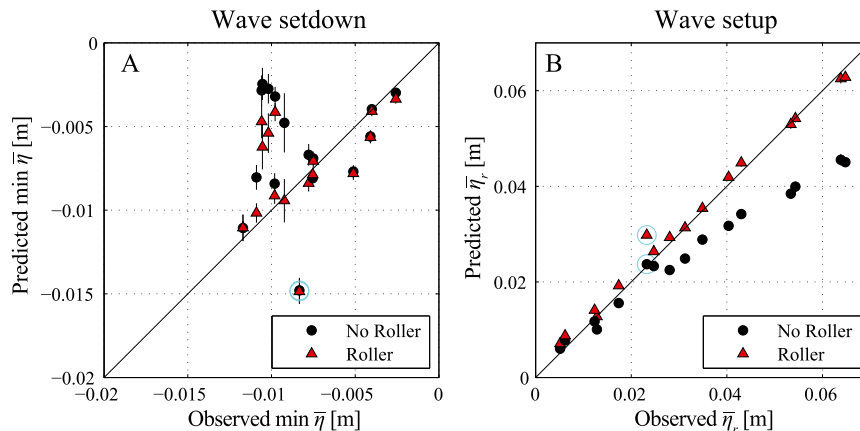
FIG. 9. Comparison of predicted wave (a) setdown and (b) setup with observations. Predictions are evaluated from Eq. (13) without (i.e., S_{xx}) and with (i.e., $S_{xx} + R_{xx}$) the wave-roller contribution to S_{xx}. Run 8 (discussed in the text) is highlighted by the cyan circles. Vertical and horizontal (generally not visible) error bars show the uncertainties due to instrument accuracy (see section 3c). Note the scale change between (a) and (b), which renders error bars in (b) less visible.

full cross-shore development of θ_w for run 4 (thus including nonbreaking areas). The wave front inclination angle θ_w rapidly increased in the shoaling region, reaching a maximum value of ~30° before decreasing during wave breaking. However, as we are only interested in θ_w, where there is a wave roller (i.e., in the surfzone), we spatially averaged θ_w over three surfzone wave gauges and compared the values to the optimum θ_r for each run (Fig. 12). With the exception of the

anomalous run 10 (discussed previously), despite θ_w being larger than θ_r (as it should from theory), there was a strong linear relationship of increasing θ_r with θ_w. This suggests a physical basis for assuming the wave-roller model via Eq. (7) and provides an explanation for the higher optimum β_D (by approximately a factor of 2) found here for the initially plunging waves, when compared to the optimum β_D reported by Reniers and Battjes (1997) for spilling waves.
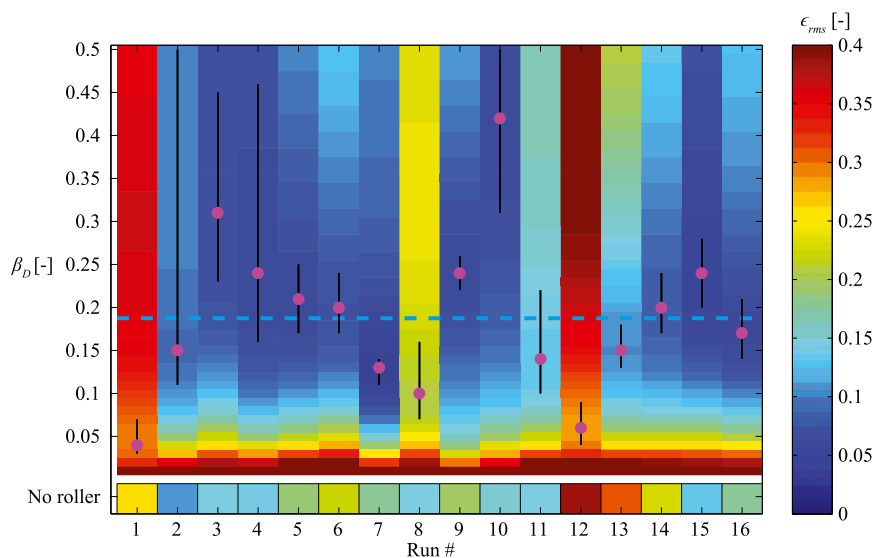
FIG. 10. Relative rms error ϵ_{rms} [Eq. (16)] in the predicted setdown/setup profiles $\overline{\eta}_{pred}$ calculated from Eq. (13) with the wave-roller contribution to radiation stress R_{xx} evaluated via Eqs. (6)–(8) using various values of the roller slope coefficient β_D. Magenta dots give the lowest ϵ_{rms} for each run, and the horizontal cyan dashed line gives the mean optimum $\beta_D = 0.19$ ($\theta_r = 11°$) for the array of runs. For comparison, ϵ_{rms} without the wave roller is shown below the main plot.
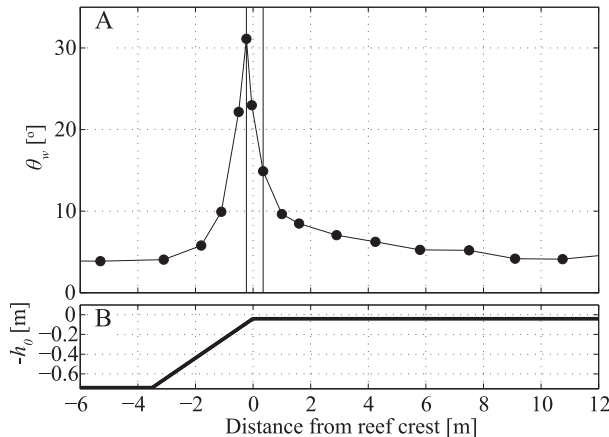
FIG. 11. (a) Estimated wave front inclination angle [θ_w; Eq. (17)] across (b) the reef profile from well offshore of the break point to near the shoreline. Vertical black lines give the averaging area used to calculate the θ_w values shown in Fig. 12.

FIG. 12. Variation of the optimum wave-roller inclination angle θ_r (the equivalent wave-roller dissipation coefficient β_D is given on the secondary y axis) with the measured wave front inclination angle θ_w [Eq. (17)] spatially averaged over the surfzone region indicated by the vertical black lines in Fig. 11.

5. Discussion

In this study, we describe the first high-resolution observations of wave transformation and wave setup/setdown through the surfzone of a steeply sloping reef profile, using a laboratory model with a bathymetry representative of many natural fringing reefs. In contrast to previous reef hydrodynamic studies, this high-resolution dataset allows us to accurately quantify the mean cross-shore momentum balances across the reef from experimental observations alone, without relying on empirical or idealized models to predict radiation stress gradients through the surfzone. We found a breakdown in the local balance between pressure gradients and radiation stress gradients (approximated from linear wave theory) within the surfzone leading to a consistent underprediction in both the wave setdown and setup (Figs. 4–6, 9).

From detailed PIV measurements of the velocities beneath plunging breaking waves (Govender et al. 2002), it appears that this breakdown within the surfzone of the balance between pressure gradients and radiation stress gradients derived from linear wave theory arises from inaccuracies in the theoretical description of the velocity field within breaking waves. Linear wave theory and other nonbreaking wave theories (e.g., cnoidal) assume that PE and KE are equal (Dean and Dalrymple 1991; Dean and Bender 2006; Svendsen 2006). Alternatively, wave-roller theory postulates that PE during wave breaking, which is the quantity we can most readily measure, is first converted to KE prior to being dissipated (Svendsen 1984b). The increased KE is in the form of a wave roller traveling with the breaking wave, which has been observed to quickly form after wave plunging (Okayasu et al. 1986; Bonmarin 1989; Govender et al. 2002). As shown in Fig. 3i (and further
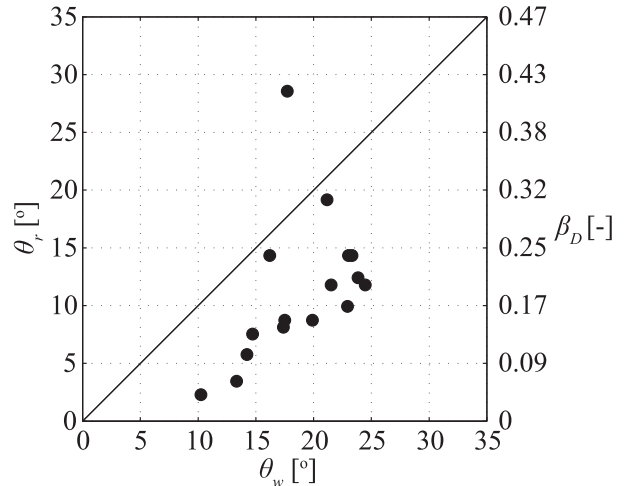
developed in Fig. 3j,k), a turbulent bore, not unlike the conceptual wave-roller model, does begin to form shortly after the initial plunging point and propagates shoreward over the horizontal reef flat. For run 4, when applying the mean water level profile with Eq. (14), this indicates that 70% of the decay of S_{xx} occurs on the horizontal reef flat, not on the reef slope. This is in agreement with results with the wave roller included (where ~65% of the decay of $S_{xx} + R_{xx}$ occurs on the reef flat) but inconsistent with the results using linear wave theory alone (where only ~35% of S_{xx} decays on the reef flat). Thus, despite wave plunging occurring on the steep reef slope (Figs. 2, 3), our results indicate that a large portion of the decrease in PE observed during the initial wave plunging is transferred shoreward onto the reef flat as KE in the form of the wave roller. This mechanism allows for KE > PE in the surfzone, which although inconsistent with nonbreaking wave theories is required to locally balance pressure gradients through the surfzone for the majority of the runs (Figs. 4, 5, 8).

Despite the wave roller being based on a simple conceptual model, we found that including the wave roller improved the local closure of the cross-shore mean momentum balances (Figs. 8b,d) and thereby predictions of both setdown and setup (Figs. 4d, 5b, 9). Run 16 (Figs. 5c,d) gives an example of the maximum magnitudes of setdown and setup being well predicted without the wave roller; however, even for this run the agreement with the observed setdown/setup profile (not just $\overline{\eta}_r$) is improved by including the wave roller. Indeed, the only runs where the wave roller did not improve

setup predictions were for runs approaching a surging breaker type ($\xi_0 \gtrsim 2.3$).

The wave-roller model implemented here includes a single parameter $\beta_D = \sin\theta_r\cos\theta_r$ (Dally and Brown 1995). From video analysis, Govender et al. (2002) reported a physical dependence of θ_r on the breaker type, with plunging waves reported to have larger θ_r than spilling waves. Thus, consistent with the measurements of Govender et al. (2002), we found the optimum value of $\beta_D = 0.19$ for the plunging waves in this study to be larger than $\beta_D = 0.1$ found by Reniers and Battjes (1997) for spilling waves on their milder-sloping beach with $\xi_0 < 0.4$ (Fig. 10). The higher optimum β_D value would thus increase the dissipation rate of the wave roller compared to Reniers and Battjes (1997). Optimum values of β_D for individual runs (Fig. 12) also displayed a strong linear relationship between the related θ_r and the measured wave front inclination angle θ_w in the surfzone, further supporting that there is a physical basis for assuming a wave roller on this steeply sloping reef profile.

The predicted wave setup on the reef flat was increased by 14%–43% by including the wave roller with the most pronounced increases for runs with large setup (i.e., for runs having large incident wave heights and low still water depths). Wave setup was on average underpredicted by 28% when using linear wave theory alone to approximate radiation stress gradients for the four runs with the largest setup (runs 5, 6, 13, and 14). Including the wave roller reduced the underprediction to just 1.5%. These particular runs would have field-scale wave heights over 4 m, which are very typical of those experienced during large storms (e.g., Stephens and Ramsay 2014). As such, caution should be used when relying on results from linear wave theory approximations alone to predict setup, especially during the large wave conditions that are often the most important for coastal hazard assessments. We also note that Apotsos et al. (2007) used Eq. (7) to model the wave roller on a mild-sloping sandy beach profile (~1/100 slope) under more moderate wave conditions ($H_{rms} = 0.2$ to 2.1 m). Under these conditions, Apotsos et al. (2007) reported on average only an 11% increase in the predicted wave setup when including the wave roller. However, as we found here for the fringing reef profile, it is possible that further investigation of the effect of the wave roller on mild-slope sandy beaches could very well reveal an increased importance of the wave roller for much larger wave conditions than were considered in that study.

Similar to the imbalance between pressure and radiation stress gradients shown here for linear wave theory, phase-resolving numerical wave models, which include nonlinear effects but not overturning (e.g., those based on the nonlinear shallow water or Boussinesq equations)

have also shown discrepancies in predicted wave setup on sleep slopes despite matching wave height observations (Skotner and Apelt 1999; Stansby and Feng 2004; Yao et al. 2012). As we show for our observations that include a wave roller, these discrepancies are likely the result of not accurately modeling the KE of waves shoreward of wave plunging point. Indeed, Stansby and Feng (2004) showed that on the steep ~1:4 slopes of sea dikes, model predictions of wave setup could be improved by including a wave roller in their nonlinear shallow-water wave model. It appears that the simple idealized model of a wave roller represents a physical correction to nonbreaking wave theory and is capable of mimicking some of the more complex dynamics of wave breaking that would otherwise require a full three-dimensional highly computationally expensive free-surface model (e.g., Torres-Freyermuth et al. 2007).

The use of a simple one-dimensional fringing reef profile with a smooth bed and an impenetrable shoreline reduced the general form of the cross-shore mean momentum equation [Eq. (1)] to a dynamic balance between the radiation stress and pressure gradients [Eq. (2)]. However, on more complex two-dimensional reef geometries that include large roughness, both nonlinear advection and bottom stresses will be nonnegligible, requiring evaluation of a more general form of Eq. (1). Nevertheless, we still expect the importance of the wave roller to accurate predictions of setup to remain. In a numerical study of varying two-dimensional reef–lagoon systems, Lowe et al. (2010) found that wave setup generation in the surfzone was dominated by radiation stress gradients, and hence the setup on the seaward portion of the reef flat was largely independent of the lagoon and channel geometries. As such, a similar setup response to what we observed using this fringing reef profile should likewise occur for more complex two-dimensional reef geometries. Similarly, incorporating wave roller formulations into a phase-resolving numerical wave model capable of modeling wave transformation on steeply sloping reefs, such as used by Yao et al. (2012) and Buckley et al. (2014), may improve numerical model predictions of wave setup. Such a model could then be used to further investigate wave setup dynamics and circulation for a much broader range of reef geometries.

An effort clearly needs to be made to more accurately measure the terms in the complete form of S_{xx} [Eq. (3)], especially within the surfzone, as this would be the greatest extension of these results. This work may also lead to further refinements in the wave-roller model, possibly including the effects of the spatially variable wave front inclination angle. However, we emphasize that the simple idealized wave-roller model used in this

study reproduced the observations exceedingly well for the majority of wave and water level conditions. Furthermore, θ_r in the wave-roller dissipation model was linearly related to the observed mean wave front inclination angle in the surfzone, indicating that there is likely a physical basis for the simple shear stress dissipation formula of Dally and Brown (1995).

6. Conclusions

High-resolution laboratory observations were used to investigate the dynamics of wave setdown and setup across a steeply sloping fringing reef profile. The one-dimensional profile with a smooth bed reduced the cross-shore mean momentum equation to a balance between the pressure and radiation stress gradients. This balance was evaluated using observations from 17 locations across the reef profile for 16 offshore wave and water level conditions. Radiation stress gradients calculated from observations using linear wave theory underpredicted setdown (8 of 16 runs; by up to 77%) and setup (12 of 16 runs; by up to 31%) with inaccuracy increasing with increased offshore wave height. For the 12 runs where setup was underpredicted (all having $H_{\text{rms},0} \geq 2.2$ m in field scale), the inclusion of a wave roller in the estimation of radiation stress gradients reduced the underprediction of setup from 21% to 3% on average. The wave roller accounts for an initial transfer of potential energy to kinetic energy during wave breaking thereby shifting the dissipation shoreward in line with pressure gradient observations. Evaluating the wave roller required a single parameter, the wave-roller inclination angle, which was found to be linearly related to our estimates of the wave front inclination angle derived from the wave gauge observations. This relationship, combined with the improved agreement with the observed setdown/setup profiles, suggests a physical basis for the wave roller. The wave roller was found to be most important for relatively large incident wave cases, therefore, under the conditions that are most critical to predict in coastal hazard assessments.

APPENDIX A

Approximation of the Time-Averaged Bottom Stress

The time-averaged bottom stress $\overline{\tau}_B$ in Eq. (1) is commonly modeled using a quadratic drag law as (e.g., Grant and Madsen 1979; Feddersen et al. 2000; Mei 2005)

$$\overline{\tau}_b = \rho C_d \overline{|u_b| u_b}, \tag{A1}$$

where u_b is the instantaneous near-bed velocity in the cross-shore direction (taken at a height just above the bottom boundary layer), and C_d is a bottom drag coefficient that depends on properties of the bottom roughness, as well as the flow environment and the height above the bed at which u_b is taken. We approximate u_b as the sum of the depth- and time-averaged Eulerian velocity (below the mean water level) U_b and the instantaneous wave orbital velocity u'_b. Local continuity was used to approximate U_b as the offshore-directed velocity necessary to balance the onshore-directed mass flux above the mean water level due to finite-amplitude nonbreaking waves and wave rollers (e.g., Apotsos et al. 2007; Lentz et al. 2008). The wave velocity u'_b was approximated using synthetically generated time series (Ruessink et al. 2012), which accounted for wave energy density and mean wave period as well as the velocity asymmetry and skewness predicted from the measured water level time series.

For the case of the smooth bed, including $\overline{\tau}_b$ via Eq. (A1) with a physically meaningful C_d [i.e., $O(0.001)$ for the smooth plywood bed; e.g., Longuet-Higgins 1970] has negligible effect on the closure of the mean momentum balance or the prediction of wave setup. For example, using a large $C_d = 0.005$ when predicting wave setup via Eq. (13) resulted in only a ~4% increase in the wave setup on the reef (when compared to using $\overline{\tau}_b = 0$). Furthermore, the cross-shore integrated residual of the pressure and radiation stress gradients varied about zero, and no significant correlation was found between the integrated residual and the integrated velocity term $\int \rho \overline{|u_b| u_b} \, dx$ (e.g., Feddersen et al. 2003). These findings indicate that for the smooth bed, the time-averaged bottom stress $\overline{\tau}_b$ was negligible for all runs (when compared to the radiation stress gradient), so for this study $\overline{\tau}_b = 0$ was used. However, this will not generally be the case, particularly for coral reefs, where the bottom roughness (and hence C_d) can be large.

APPENDIX B

Separation of Shoreward- and Seaward-Propagating Waves

A frequency domain algorithm (assuming linear wave theory) was used to separate shoreward-propagating ($^+$) and seaward-propagating ($^-$) wave motion from synchronous velocity and water level time series. The shoreward-propagating F_η^+ and seaward-propagating F_η^- Fourier components of a water level time series are related to the observed "total" Fourier components as $F_\eta = F_\eta^+ + F_\eta^-$; likewise, for the velocity components $F_u = F_u^+ + F_u^-$. Using the kinematic relationship between wave height and velocity gives

$$F_u^+ = \frac{gk}{2\pi f} K_u F_\eta^+, \quad \text{and}$$

$$F_u^- = -\frac{gk}{2\pi f} K_u F_\eta^-, \tag{B1}$$

where k (f) is the wavenumber, and K_u (f) is the linear wave theory velocity response function, defined as

$$K_u = \frac{\cosh(kh_u)}{\cosh[k(h_0 + \overline{\eta})]}, \tag{B2}$$

in which h_u is the height above the bed where velocity is measured. This gives a system of four equations with four unknown variables (F_η^+, F_η^- and F_u^+, F_u^-); rearranging yields equations for F_η^+ and F_η^- as

$$F_\eta^+ = \frac{1}{2}\left(F_\eta + \frac{2\pi f}{gkK_u} F_u\right), \quad \text{and}$$

$$F_\eta^- = \frac{1}{2}\left(F_\eta - \frac{2\pi f}{gkK_u} F_u\right). \tag{B3}$$

The inverse Fourier transformations of F_η^+ and F_η^- were used to generate time series of the shoreward- and seaward-propagating components of the wave signals, respectively.

REFERENCES

Apotsos, A., B. Raubenheimer, S. Elgar, R. T. Guza, and J. A. Smith, 2007: Effects of wave rollers and bottom stress on wave setup. *J. Geophys. Res.*, **112**, C02003, doi:10.1029/2006JC003549.

Baldock, T. E., A. Golshani, D. P. Callaghan, M. I. Saunders, and P. J. Mumby, 2014: Impact of sea-level rise and coral mortality on the wave dynamics and wave forces on barrier reefs. *Mar. Pollut. Bull.*, **83**, 155–164, doi:10.1016/j.marpolbul.2014.03.058.

Battjes, J. A., 1972: Radiation stresses in short-crested waves. *J. Mar. Res.*, **30**, 56–64.

——, 1974: Surf similarity. *Proc. 14th Conf. on Coastal Engineering*, Copenhagen, Denmark, ASCE, 466–480.

——, 1988: Surf-zone dynamics. *Annu. Rev. Fluid Mech.*, **20**, 257–293, doi:10.1146/annurev.fl.20.010188.001353.

——, and M. J. F. Stive, 1985: Calibration and verification of a dissipation model for random breaking waves. *J. Geophys. Res.*, **90**, 9159–9167, doi:10.1029/JC090iC05p09159.

Becker, J. M., M. A. Merrifield, and M. Ford, 2014: Water level effects on breaking wave setup for Pacific Island fringing reefs. *J. Geophys. Res. Oceans*, **119**, 914–932, doi:10.1002/2013JC009373.

Bonmarin, P., 1989: Geometric-properties of deep-water breaking waves. *J. Fluid Mech.*, **209**, 405–433, doi:10.1017/S0022112089003162.

Booij, N., R. C. Ris, and L. H. Holthuijsen, 1999: A third-generation wave model for coastal regions: 1. Model description and validation. *J. Geophys. Res.*, **104**, 7649–7666, doi:10.1029/98JC02622.

Bouws, E., H. Gunther, W. Rosenthal, and C. L. Vincent, 1985: Similarity of the wind wave spectrum in finite depth water: 1. Spectral form. *J. Geophys. Res.*, **90**, 975–986, doi:10.1029/JC090iC01p00975.

Bowen, A. J., D. L. Inman, and V. P. Simmons, 1968: Wave set-down and set-up. *J. Geophys. Res.*, **73**, 2569–2577, doi:10.1029/JB073i008p02569.

Buckley, M., R. Lowe, and J. Hansen, 2014: Evaluation of near-shore wave models in steep reef environments. *Ocean Dyn.*, **64**, 847–862, doi:10.1007/s10236-014-0713-x.

Dally, W. R., and C. A. Brown, 1995: A modeling investigation of the breaking wave roller with application to cross-shore currents. *J. Geophys. Res.*, **100**, 24 873–24 883, doi:10.1029/95JC02868.

Dean, R. G., and R. A. Dalrymple, 1991: *Water Wave Mechanics for Engineers and Scientist*. Advanced Series on Ocean Engineering, Vol. 2, World Scientific, 368 pp.

——, and C. J. Bender, 2006: Static wave setup with emphasis on damping effects by vegetation and bottom friction. *Coastal Eng.*, **53**, 149–156, doi:10.1016/j.coastaleng.2005.10.005.

Duncan, J. H., 1981: An experimental investigation of breaking waves produced by a towed hydrofoil. *Proc. Roy. Soc. London*, **A377**, 331–348, doi:10.1098/rspa.1981.0127.

Eslami Arab, S., A. van Dongeren, and P. Wellens, 2012: Studying the effect of linear refraction on low-frequency wave propagation (physical and numerical study). *Proc. 33rd Conf. on Coastal Engineering*, Santander, Spain, Coastal Engineering Research Council, waves.9, doi:10.9753/icce.v33.waves.9.

Falter, J. L., R. J. Lowe, Z. L. Zhang, and M. McCulloch, 2013: Physical and biological controls on the carbonate chemistry of coral reef waters: Effects of metabolism, wave forcing, sea level, and geomorphology. *PLoS One*, **8**, e53303, doi:10.1371/journal.pone.0053303.

Feddersen, F., 2004: Effect of wave directional spread on the radiation stress: Comparing theory and observations. *Coastal Eng.*, **51**, 473–481, doi:10.1016/j.coastaleng.2004.05.008.

——, R. T. Guza, S. Elgar, and T. H. C. Herbers, 2000: Velocity moments in alongshore bottom stress parameterizations. *J. Geophys. Res.*, **105**, 8673–8686, doi:10.1029/2000JC900022.

——, E. L. Gallagher, R. T. Guza, and S. Elgar, 2003: The drag coefficient, bottom roughness, and wave-breaking in the nearshore. *Coastal Eng.*, **48**, 189–195, doi:10.1016/S0378-3839(03)00026-7.

Gourlay, M. R., 1996: Wave set-up on coral reefs. 2. Set-up on reefs with various profiles. *Coastal Eng.*, **28**, 17–55, doi:10.1016/0378-3839(96)00009-9.

Govender, K., G. P. Mocke, and M. J. Alport, 2002: Video-imaged surf zone wave and roller structures and flow fields. *J. Geophys. Res.*, **107**, doi:10.1029/2000JC000755.

——, H. Michallet, M. J. Alport, U. Pillay, G. P. Mocke, and M. Mory, 2009: Video DCIV measurements of mass and momentum fluxes and kinetic energies in laboratory waves breaking over a bar. *Coastal Eng.*, **56**, 876–885, doi:10.1016/j.coastaleng.2009.04.002.

Grant, W. D., and O. S. Madsen, 1979: Combined wave and current interaction with a rough bottom. *J. Geophys. Res.*, **84**, 1797–1808, doi:10.1029/JC084iC04p01797.

Grilli, S. T., I. A. Svendsen, and R. Subramanya, 1997: Breaking criterion and characteristics for solitary waves on slopes. *J. Waterw. Port Coastal Ocean Eng.*, **123**, 102–112, doi:10.1061/(ASCE)0733-950X(1997)123:3(102).

Iwata, K., and T. Tomita, 1992: Variation of potential and kinetic wave energy in surf zone. *Proc. 23rd Int. Conf. Coastal Engineering*, Venice, Italy, ASCE, 336–349.

Lentz, S., and B. Raubenheimer, 1999: Field observations of wave setup. *J. Geophys. Res.*, **104**, 25 867–25 875, doi:10.1029/1999JC900239.

——, M. Fewings, P. Howd, J. Fredericks, and K. Hathaway, 2008: Observations and a model of undertow over the inner continental shelf. *J. Phys. Oceanogr.*, **38**, 2341–2357, doi:10.1175/2008JPO3986.1.

Longuet-Higgins, M. S., 1970: Longshore currents generated by obliquely incident sea waves: 1. *J. Geophys. Res.*, **75**, 6778, doi:10.1029/JC075i033p06778.

——, and R. W. Stewart, 1962: Radiation stress and mass transport in gravity waves, with application to 'surf beats.' *J. Fluid Mech.*, **13**, 481–504, doi:10.1017/S0022112062000877.

——, and ——, 1964: Radiation stresses in water waves; A physical discussion, with applications. *Deep-Sea Res. Oceanogr. Abstr.*, **11**, 529–562, doi:10.1016/0011-7471(64)90001-4.

Lowe, R. J., and J. L. Falter, 2015: Oceanic forcing of coral reefs. *Annu. Rev. Mar. Sci.*, **7**, 43–66, doi:10.1146/annurev-marine-010814-015834.

——, ——, S. G. Monismith, and M. J. Atkinson, 2009: A numerical study of circulation in a coastal reef-lagoon system. *J. Geophys. Res.*, **114**, C06022, doi:10.1029/2008JC005081.

——, C. Hart, and C. B. Pattiaratchi, 2010: Morphological constraints to wave-driven circulation in coastal reef-lagoon systems: A numerical study. *J. Geophys. Res.*, **115**, C09021, doi:10.1029/2009JC005753.

Massel, S. R., and M. R. Gourlay, 2000: On the modelling of wave breaking and set-up on coral reefs. *Coastal Eng.*, **39**, 1–27, doi:10.1016/S0378-3839(99)00052-6.

Mei, C. C., 2005: *Theory and Applications of Ocean Surface Waves.* Advanced Series on Ocean Engineering, Vol. 23, World Science, 1136 pp.

Monismith, S. G., 2007: Hydrodynamics of coral reefs. *Annu. Rev. Fluid Mech.*, **39**, 37–55, doi:10.1146/annurev.fluid.38.050304.092125.

Okayasu, A., T. Shibayama, and N. Mimura, 1986: Velocity field under plunging waves. *Proc. 20th Conf. on Coastal Engineering*, Taipei, Taiwan, ASCE, 660–674.

Phillips, O. M., 1977: The Dynamics of the Upper Ocean. *Cambridge Monogr. Mech. Appl. Math.*, Vol. 2, Cambridge University Press, 344 pp.

Raubenheimer, B., R. T. Guza, and S. Elgar, 2001: Field observations of wave-driven setdown and setup. *J. Geophys. Res.*, **106**, 4629–4638, doi:10.1029/2000JC000572.

Reniers, A. J. H. M., and J. A. Battjes, 1997: A laboratory study of longshore currents over barred and non-barred beaches. *Coastal Eng.*, **30**, 1–21, doi:10.1016/S0378-3839(96)00033-6.

Ruessink, B. G., G. Rarnaekers, and L. C. van Rijn, 2012: On the parameterization of the free-stream non-linear wave orbital motion in nearshore morphodynamic models. *Coastal Eng.*, **65**, 56–63, doi:10.1016/j.coastaleng.2012.03.006.

Sheppard, C., D. J. Dixon, M. Gourlay, A. Sheppard, and R. Payet, 2005: Coral mortality increases wave energy reaching shores protected by reef flats: Examples from the Seychelles. *Estuarine Coastal Shelf Sci.*, **64**, 223–234, doi:10.1016/j.ecss.2005.02.016.

Skotner, C., and C. J. Apelt, 1999: Application of a Boussinesq model for the computation of breaking waves: Part 2: Wave-induced setdown and setup on a submerged coral reef. *Ocean Eng.*, **26**, 927–947, doi:10.1016/S0029-8018(98)00062-6.

Smith, J. A., 2006: Wave–current interactions in finite depth. *J. Phys. Oceanogr.*, **36**, 1403–1419, doi:10.1175/JPO2911.1.

Stansby, P. K., and T. Feng, 2004: Surf zone wave overtopping a trapezoidal structure: 1-D modelling and PIV comparison. *Coastal Eng.*, **51**, 483–500, doi:10.1016/j.coastaleng.2004.06.001.

Stephens, S. A., and D. L. Ramsay, 2014: Extreme cyclone wave climate in the southwest Pacific Ocean: Influence of the El Niño Southern Oscillation and projected climate change. *Global Planet. Change*, **123**, 13–26, doi:10.1016/j.gloplacha.2014.10.002.

Stive, M. J. F., and H. G. Wind, 1982: A study of radiation stress and set-up in the nearshore region. *Coastal Eng.*, **6**, 1–25, doi:10.1016/0378-3839(82)90012-6.

——, and H. J. De Vriend, 1994: Shear stresses and mean flow in shoaling and breaking waves. *Proc. 24th Conf. on Coastal Engineering*, Kobe, Japan, ASCE, 594–608.

Storlazzi, C. D., E. Elias, M. E. Field, and M. K. Presto, 2011: Numerical modeling of the impact of sea-level rise on fringing coral reef hydrodynamics and sediment transport. *Coral Reefs*, **30**, 83–96, doi:10.1007/s00338-011-0723-9.

Svendsen, I. A., 1984a: Wave heights and set-up in a surf zone. *Coastal Eng.*, **8**, 303–329, doi:10.1016/0378-3839(84)90028-0.

——, 1984b: Mass flux and undertow in a surf zone. *Coastal Eng.*, **8**, 347–365, doi:10.1016/0378-3839(84)90030-9.

——, 2006: *Introduction to Nearshore Hydrodynamics.* Advanced Series on Ocean Engineering, Vol. 24, World Science, 744 pp.

——, and U. Putrevu, 1993: Surf zone wave parameters from experimental data. *Coastal Eng.*, **19**, 283–310, doi:10.1016/0378-3839(93)90033-5.

Torres-Freyermuth, A., I. J. Losada, and J. L. Lara, 2007: Modeling of surf zone processes on a natural beach using Reynolds-averaged Navier-Stokes equations. *J. Geophys. Res.*, **112**, C09014, doi:10.1029/2006JC004050.

van Dongeren, A., G. Klopman, A. Reniers, and H. Petit, 2002: High-quality laboratory wave generation for flumes and basins. *Ocean Wave Measurement and Analysis (*2001*)*, B. L. Edge and J. M. Hemsley, Eds., American Society of Civil Engineers, 1190–1199, doi:10.1061/40604(273)120.

Vetter, O., J. M. Becker, M. A. Merrifield, A. C. Pequignet, J. Aucan, S. J. Boc, and C. E. Pollock, 2010: Wave setup over a Pacific Island fringing reef. *J. Geophys. Res.*, **115**, C12066, doi:10.1029/2010JC006455.

Yao, Y., Z. H. Huang, S. G. Monismith, and E. Y. M. Lo, 2012: 1DH Boussinesq modeling of wave transformation over fringing reefs. *Ocean Eng.*, **47**, 30–42, doi:10.1016/j.oceaneng.2012.03.010.